

Single Boron Atom Anchored on graphitic carbon nitride nanosheet (B/g-C₂N) as a photocatalyst for Nitrogen fixation: A First-Principles Study

Hao-Ran Zhu, Shi-Hao Wei and Da-Yin Hua

Department of Microelectronic Science and Engineering,

*School of Physical Science and Technology, Ningbo University, Ningbo, 315211, P.R. China**

(Dated: October 21, 2019)

Photocatalytic nitrogen reduction is the promising way for ammonia production, the question now is that the search of highly active and low active catalysts. Based on the first-principles calculation, single boron atom is anchored on the g-C₂N to form B/g-C₂N, the results show that B/g-C₂N can serve as a potential photocatalyst for N₂ fixation. The introduction of B atom to g-C₂N, the energy gap will reduce from 2.45 eV to 1.21 eV, and also show strong absorption in the visible light region. In addition, N₂ can be efficiently reduced on B/g-C₂N through the enzymatic mechanism with low onset potential of 0.07 V and rate-determining barrier of 0.50 eV. The “acceptance-donation” interaction between B/g-C₂N and N₂ plays a key role to active N₂, the BN₂ moiety of B/g-C₂N acts as active and transportation center. And the activity originates from the strong interaction between $1\pi 1\pi^*$ orbitals of N₂ and molecular orbitals of B/g-C₂N, the ionization of 1π orbital and the filling of $1\pi^*$ orbital can increase the N \equiv N bond length greatly, making the activation of N₂. Overall, this work demonstrates B/g-C₂N is a promising photocatalyst for N₂ fixation.

PACS numbers:

I. INTRODUCTION

Ammonia (NH₃) is not only an important chemical in agriculture and industry fields but also a potential energy storage intermediate due to its high energy density, safe and environment ecofriendly[1–4]. Currently, the industrial NH₃ production mainly relies on the Haber-Bosch process with Fe- or Ru-based catalysts, which involves harsh conditions (typically 300-500 °C and 200-300 atm), yielding roughly 500 million tons per year, accompanied by the heavy energy consumption, necessary H₂ feedstock from fossil fuel and a large number of greenhouse gases emission[3, 5, 6]. Thus, it is of great significance to develop a green and sustainable strategy for NH₃ production[7]. The proton-assisted photocatalytic or electrocatalytic N₂ reduction reaction (NRR), ideally under ambient conditions using renewable solar and wind energy, has been proposed as a promising alternative for nitrogen fixation and ammonia production, which stem from N₂ biological fixation with nitrogenase enzymes in bacteria that perform nitrogen fixation at room temperature and atmospheric pressure[3, 6, 8–11]. For instance, photo(electro)catalytic NRR can be directly driven the sunlight[4, 6]. Thus, these two strategies are highly promising for achieving clean, carbon-free and sustainable NH₃ production from N₂.

Up to now, numerous catalysts have been fabricated for N₂ fixation, such as Ru, graphene, MXene, metal oxides, and so on[12–17]. Although NRR catalysts based on noble metals (e.g., Au_{27,28}, Ru₂₉, Rh₃₀) show favorable activity, but the scarcity and high cost hinder the widespread application. Compared to metal based cat-

alysts, metal-free catalysts can possess the fact that excellent activity, long durability, and intrinsic advantages of low cost and environmental friendliness[14, 16, 18–29]. Recently, boron-doped graphene shows NH₃ production rate can reach up to 9.8 g*hr⁻¹*cm⁻² with a high FE of 10.8% at 0.5 V versus RHE) in aqueous solutions at ambient conditions[14]. B₄C nanosheet achieves a high NH₃ yield of 26.57 g*h⁻¹ mg⁻¹ and a high FE of 15.95% at a potential of -0.75 V in 0.1 M HCl[16]. The development of efficient metal-free catalysts for NRR of great economic interest and scientific importance. In 2015, a novel 2D layered crystal with uniformly distributed holes, graphitic carbon nitride named g-C₂N was successfully prepared by a simple bottom-up wet chemical method[30]. The native porous structure of g-C₂N makes it the excellent substrate to support single-atom catalysts (SACs). At present, the N-containing big holes could anchor TM atoms tightly to carry out a series of electro-catalytic reaction like hydrogen evolution reaction (HER)[31, 32], oxygen evolution reaction (OER)[32, 33] and N₂ reduction reaction (NRR)[34]. Also, the moderate energy gap make it suitable for the application for photocatalysts.

In this work, we employ first-principles computations to design single boron atom anchored g-C₂N monolayers (B/g-C₂N) and explore their catalytic performance towards N₂ reduction. As expected, the decoration of B atom on g-C₂N can maintain and enhance slightly the visible light absorption, making the reduction process possibly occur under visible light. In addition, comparing to insufficient ability of g-C₂N to adsorb N₂, B/g-C₂N can bind the N₂ strongly, with binding energies of -0.57 eV and -1.40 eV through side-on and end-on patterns, respectively. Surprisingly, the adsorbed N₂ can be further reduced into NH₃ with a rather low onset potential of 0.07 V and free energy barrier of 0.50 eV through the en-

*Electronic address: weishihao@nbu.edu.cn

zymatic mechanism. The stability of B/g-C₂N is systematically evaluated and shows that the designed catalyst is very promising to be synthesized.

II. CALCULATION DETAILS

The spin-polarized DFT calculations are performed by using Vienna Ab initio Simulation Package (VASP)[35, 36] with projector-augmented-wave (PAW) pseudopotentials[37]. The generalized gradient approximation (GGA) in the form of the Perdew-Burke-Ernzerhof (PBE)[38, 39] is used for treating the electronic exchange-correction interactions and a cutoff energy of 500 eV for the plane-wave expansion is adopted. The convergence threshold is 10^{-5} eV and 0.01 eV/Å for energy and force, respectively. A vacuum space is larger than 20 Å, which is set to avoid interactions between two periodic units. The single-atom catalyst are modeled by depositing one B atom on $2 \times 2 \times 1$ supercell g-C₂N, Brillouin zones are sampled by a Monkhorst-Pack k-point mesh with a $3 \times 3 \times 1$ k-point grid. In order to better describe the long-range van der Waals interaction, the DFT-D2 correction[40] proposed by Grimme and co-workers is applied. Hybrid functionals based on the Heyd-Scuseria-Ernzerhof (HSE06) method[41] are employed to obtain the exact band structures and optical absorption spectra. The climbing nudged elastic band (CI-NEB) method[42] as implemented in VTST tools is carried out to search the transition states and saddle points along the reaction pathway, and the activation barriers for electrochemical reaction are calculated using a transferable method reported by Janik et al.[43] Ab initio molecular dynamics simulation (AIMD) by Forcite code[44] with isobaric-isothermal (NPT) ensemble is employed to evaluate the thermodynamic stability of the materials, the simulation is run under 1000 K for 100 ps with time step of 2 fs.

The calculations of Gibbs free energy change (ΔG) for each elemental step are based on the computational hydrogen electrode model proposed by Nørskov et al.,[45, 46] which can be determined as follows:

$$\Delta G = \Delta E + \Delta E_{ZPE} - T\Delta S + \Delta G_U + \Delta G_{pH} \quad (1)$$

where ΔE is the difference between the adsorption energies of a given group; ΔE_{ZPE} and ΔS are the changes in zero point energies and entropy, severally, T is the temperature, which is set to be 298.15 K in this work, ΔG_U is the contributions of electrode potential to shift the free energy ΔG at the applied electrode potential (U); ΔG_{pH} is the free energy correction of pH ($\Delta G_{pH} = 2.303 \times k_B T \times pH \approx 0.059 \times pH$), the pH value is set to be zero in this work. The E_{ZPE} and TS for each reaction intermediates can be calculated from the vibrational frequencies, via the following equation:

$$E_{ZPE} = \frac{1}{2} \sum_{i=1}^n h\nu_i \quad (2)$$

$$TS = TR \sum_{i=1}^n \left\{ \frac{hc\tilde{\nu}_i}{k_b T (e^{\frac{hc\tilde{\nu}_i}{k_b T}} - 1)} - \ln(1 - e^{-\frac{hc\tilde{\nu}_i}{k_b T}}) \right\} \quad (3)$$

where R , h , c , k_b , ν and $\tilde{\nu}$ are gas constant, Planck constant, light speed, Boltzmann constant, vibrational frequencies and wave number, respectively. Moreover, only the calculation of zero point energy and entropy of reaction intermediates are needed and the contribution of substrate can be offset. The entropies and zero-point energies of molecules in the gas phase are obtained from the NIST database.[<http://cccbdb.nist.gov/>]

III. RESULTS AND DISCUSSION

A. B-doped g-C₂N

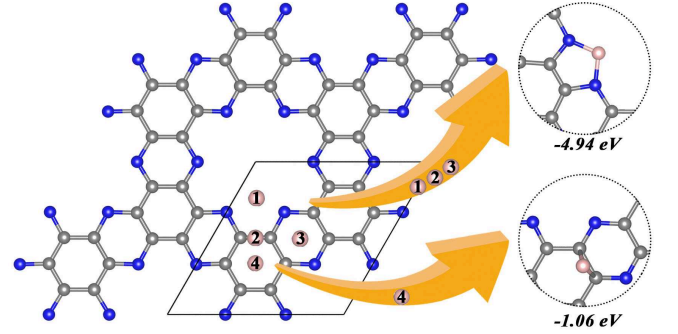


FIG. 1: Initial structures of B atom adsorbed on g-C₂N at different sites (at the left panel), and their optimized structures are illustrated on the right panel. The gray, lightpink, and blue balls represent C, B and N atoms, respectively.

As shown in Figure 1, on account of the larger radius of B atom than that of C and N atoms, there are 4 rational types of adsorption site for the adsorption of B atom in g-C₂N: type-1 is located at the linkage site of two nitrogen atoms, type-2 is positioned in the bridge site of C atom, type-3 corresponds to the middle of six-membered ring which including two N atoms and four C atoms, and type-4 is the middle of six-membered ring of carbon atoms. B atom is added in each kind of adsorption sites. After optimization of these adsorption structures, the type-2 and type-3 transfer to the type-1, and the binding energy is calculated to be -4.94 eV, as for the type-4, B atom moves to the bridge site of C atom and also has negative binding energy of -1.06 eV (Figure 1). Obviously, the binding energy of type-1 is most favorable in energy. High binding energy and large energy difference of the formation energies between the different adsorption types of the B/g-C₂N provides significant advantages in terms of experimental synthesis, so the following researches focus on the structure of type-1.

The deposition of B atom on g-C₂N can significantly modify its electronic structure, Figure 2(a)-(c) presents

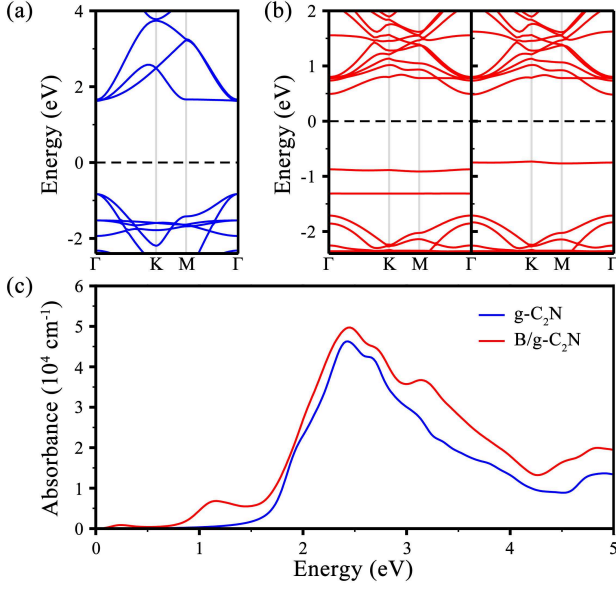


FIG. 2: The Band structures of (a) g-C₂N and (b) B/g-C₂N with spin up (left) and spin down (right). (c) The optical absorption spectra of g-C₂N and B/g-C₂N. The Fermi level is represented by dash line and set to 0 eV.

the band structures and optical adsorption spectra of pristine g-C₂N and B/g-C₂N. The band gap of g-C₂N is calculated to be 2.45 eV, which is in accordance with the previous theoretical results[47, 48]. With B atom depositing on the g-C₂N, introducing a impurity energy level come from B atom lie in the midst of band gap of g-C₂N. Therefore, the band gap of B/g-C₂N is significant reducing to 1.21 eV, and the non-magnetic g-C₂N will possess the magnetic moment of 1 μ_B when B atom interact with two N atoms of g-C₂N (moiety of BN₂). In order to achieve high-efficiency application in photocatalytic materials, wide and strong optical absorption in the optimal visible-light regions is naturally expected. Thus, we further investigate the optical absorption spectra for the g-C₂N and B/g-C₂N monolayers. As shown in Figure 2(c), it is noted that the introduction of B atom is found to be further extended the absorption edge to the infrared light region and enhance the visiblelight absorption efficiency slightly, indicating that visible-light utilization of the B/g-C₂N is a little more efficient than that of the pure g-C₂N monolayer.

B. N₂ molecule adsorbed on B/g-C₂N

As we all known, N₂ is adsorbed on catalysts via side-on and end-on adsorption patterns. Therefore, the interaction between N₂ and B/g-C₂N is investigated. For N₂ adsorbed on the B/g-C₂N, N₂ can only adsorb to B atom of the moiety of BN₂ with the release of energy, and the occupied orbital and unoccupied orbital of BN₂

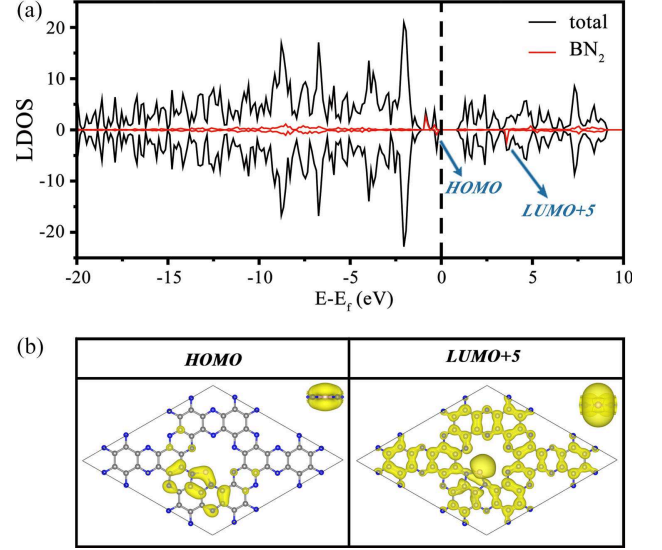


FIG. 3: (a) Spin-polarized local density of state (LDOS) of B/g-C₂N. (b) The highest occupied molecular orbital (HOMO) and sixth-lowest unoccupied molecular orbital (LUMO+5) of B/g-C₂N, where the isosurface value is set to be 0.001 e/Å³. The gray, lightpink, and blue balls represent C, B and N atoms, respectively. The insert shows the orbital of moiety of BN₂ on side view.

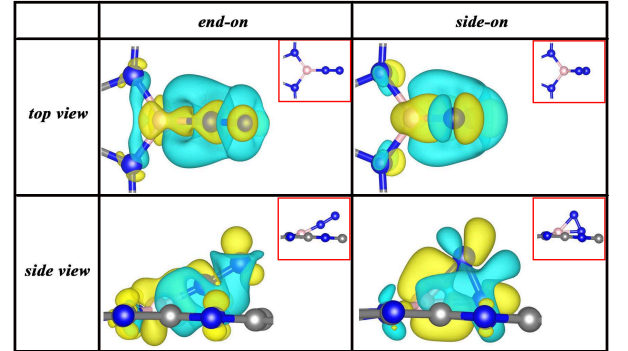


FIG. 4: Difference charge density of N₂ adsorbed on B/g-C₂N, where the isosurface value is set to be 0.02 e/Å³. The charge accumulation and depletion are shown in yellow and cyan, respectively. The gray, lightpink, and blue balls represent C, B and N atoms, respectively.

near the E_f lie in the highest occupied molecular orbital (HOMO) and sixth-lowest unoccupied molecular orbital (LUMO+5) of B/g-C₂N (Figure 3 and S1). And the difference charge density of N₂ adsorbed on B/g-C₂N are plotted in Figure 4. Adsorption energy (E_{ads}^{N₂}, in eV) and bond Length (d_{N-N}, in Å) of N₂ adsorbed on B/g-C₂N; bader charge transfer ($\Delta\rho$) from B/g-C₂N to N₂; Minimum Energy Reaction Pathway (MERP); Rate-Limiting Step (RLS) and onset potential (U, in V) for the electrocatalytic reaction of N₂ reduction to NH₃ on B/g-C₂N are also listed in Table 1. The shapes of HOMO and

TABLE I: Adsorption energy ($E_{ads}^{N_2}$, in eV) and bond length (d_{N-N} , in Å) of N_2 adsorbed on B/g- C_2N ; bader charge transfer ($\Delta\rho$) from B/g- C_2N to N_2 ; Minimum Energy Reaction Pathway (MERP); Rate-Limiting Step (RLS) and onset potential (U, in V) for the electrocatalytic reaction of N_2 reduction to NH_3 on B/g- C_2N .

Adsorption pattern	$E_{ads}^{N_2}$ (ΔG_{N_2})	d_{N-N} ($\Delta\rho$)	MERP	RLS	U
end-on	-1.40 (-0.82)	1.13 (0.39)	pathway V	*N-NH ₂ → *N	0.74
side-on	-0.57 (-0.02)	1.20 (0.73)	pathway V	*N-*NH → *N-*NH ₂	0.07

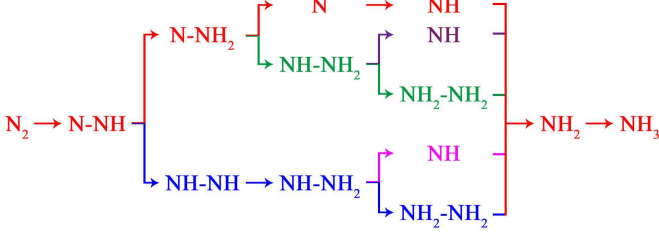


FIG. 5: Proposed schematic elementary reactions for N_2 reduction to NH_3 on B/g- C_2N . The red, purple, green, magenta and blue lines represent the reaction pathways I, II, III, IV and V, respectively.

LUMO+5 of the moiety of BN_2 are similar to π orbital (Figure 3), indicating that it has possibility to adsorb N_2 via side-on adsorption. This is because there are the better hybridization between N_2 and moiety of BN_2 . As expected, the binding strength between N_2 and B/g- C_2N is exothermic process with the adsorption free energy of -0.82 and -0.02 eV for end-on and side-on adsorption, respectively. Due to N_2 molecule has a lone pair of electrons and the moiety of BN_2 has partially occupied π orbitals, it can be expected that the interaction between N_2 and BN_2 is “acceptance-donation” mechanism. As shown in Figure 4, the charge density difference of B/g- C_2N with the adsorption of N_2 is calculated to clarify the interaction between B/g- C_2N and N_2 . Interestingly, the “acceptance-donation” process is found here, which charge accumulation and depletion can be observed for both N_2 molecule and B/g- C_2N , indicating the N_2 can not only accept electrons from B/g- C_2N , but also donate electrons to B/g- C_2N . Obviously, comparing to donate electrons, N_2 tend to accept electrons from B/g- C_2N (Figure 4). The bader charge analysis also shows that the N_2 gains 0.39 and 0.73 |e| from B/g- C_2N for end-on and side-on configurations, respectively (Table 1). Therefore, N_2 with side-on adsorption configuration can accept more electrons than end-on adsorption configuration, making the bond length of N_2 become longer (1.20 Å v.s 1.13 Å), the increase of $N\equiv N$ bond length implies the activation of the inert $N\equiv N$ triple bond. We note that the better orbital hybridization can be achieved when N_2 is adsorbed onto B/g- C_2N with side-on pattern. Therefore, the energy released by side-on adsorption pattern should be more than that released by end-on adsorption

pattern. However, due to the “acceptance-donation” interaction mechanism, more electrons are obtained by $1\pi^*$ anti-bonding orbital of N_2 for side-on adsorption pattern, as mentioned in our previous work[49], which will lead to the longer $N\equiv N$ bond length. Therefore, the energy released by side-on pattern is less than that released by end-on pattern, because most of the energy is used to activate the $N\equiv N$ triple bond. As expected, as shown in Table 1, the adsorption of N_2 to B/g- C_2N is an exothermic process with the adsorption free energy of -0.82 eV and -0.02 eV for end-on and side-on adsorption patterns, respectively.

C. Electrocatalytic NRR

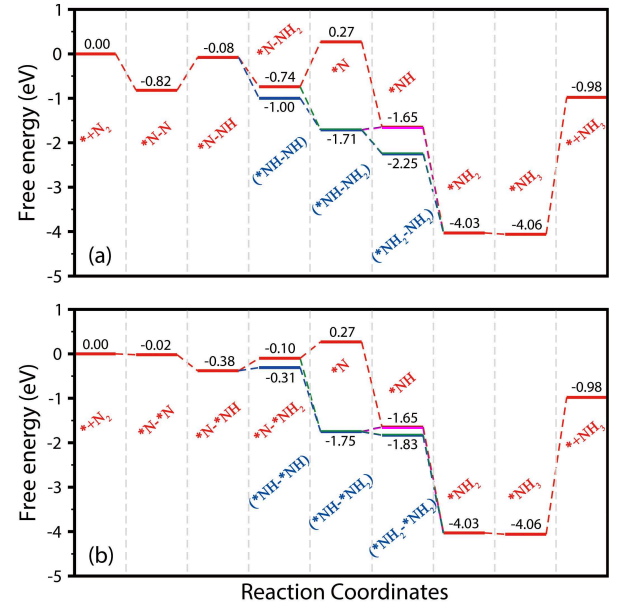


FIG. 6: Gibbs free-energy change (ΔG) for N_2 reduction to NH_3 on B/g- C_2N through (a) end-on and (b) side-on pattern. “*” denotes the catalyst (B/g- C_2N). The red, purple, green, magenta and blue lines represent the reaction pathways I, II, III, IV and V, respectively, as shown in Figure 5. The energy of the entrance, including the isolated B/g- C_2N and free N_2 molecule, is set to zero as the reference.

Generally, as shown in Figure 5, the possible reaction

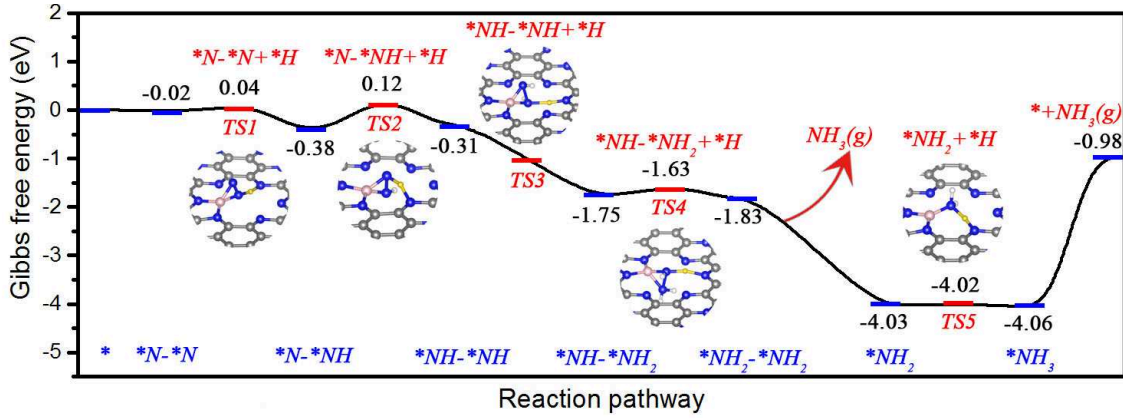


FIG. 7: Minimum energy pathway for N_2 reduction into NH_3 catalysed by B/g- C_2N through side-on pattern. The energy of the entrance, including the isolated B/g- C_2N and free N_2 molecule, is set to zero as the reference. The structures of the Transition States (TS) are indicated. The gray, lightpink, blue and white balls represent C, B, N and H atoms, respectively. The reactive hydrogen atom during the N_2 electro-reduction is highlighted in golden in each step.

pathways of N_2 reduction to NH_3 on B/g- C_2N will follow five possible reaction pathways whether the adsorption configuration is end-on or side-on adsorption pattern. The assessment of the catalytic performance about B/g- C_2N for the reduction of N_2 into NH_3 by calculating NRR is evaluated by calculating the Gibbs free energy change (ΔG) in every hydrogenation steps, and the reaction process involve six net proton coupled electron transfer (PCET) steps. Figure 6 displays all of the reaction pathways with the corresponding Gibbs free energy profile for B/g- C_2N catalyze N_2 reduction. The initial adsorption of N_2 molecule for the end-on and side-on adsorption patterns release free energy of 0.82 eV and 0.02 eV, respectively. For the end-on adsorption pattern, there is a maximum ΔG (ΔG_{max}) of 1.01 eV in the third PCET step ($^*\text{NNH}_2 + \text{H}^+/\text{e}^- \rightarrow ^*\text{N} + \text{NH}_3$) of the reaction pathway I. At the same time, as shown in Figure 65(a), a relatively small Gibbs free energy barrier of 0.06 eV is found in the fourth PCET step ($^*\text{NH}-\text{NH}_2 + \text{H}^+/\text{e}^- \rightarrow ^*\text{NH} + \text{NH}_3$) of the reaction pathway IV, and there is no Gibbs free energy barrier for the rest of hydrogenation steps. We also notice that, in the end-on pattern, all reaction pathways need to cross a larger reaction barrier (0.74 eV, the first protonation: $^*\text{N}_2 + \text{H}^+/\text{e}^- \rightarrow ^*\text{NNH}$), which means that it is very difficult for nitrogen reduction into ammonia at ambient conditions.

As for the five possible reaction pathways of the side-on adsorption configuration, as shown in Figure 6(b), the ΔG_{max} for the reaction pathway I is 0.37 eV in the third PCET step ($^*\text{N}-^*\text{NH}_2 + \text{H}^+/\text{e}^- \rightarrow ^*\text{N} + \text{NH}_3$), which is the largest ΔG_{max} among these five reaction pathways. Meanwhile, the ΔG_{max} for the reaction pathway V is 0.07 eV in the second PCET step ($^*\text{N}-^*\text{NH} + \text{H}^+/\text{e}^- \rightarrow ^*\text{NH}-^*\text{NH}$), which is the smallest ΔG_{max} among these five reaction pathways. It is worth noting that, in this reaction pathway V, every elementary steps are exothermic except for the second protonation to form $^*\text{NH}-^*\text{NH}$.

So we come to a conclusion that, for the side-on adsorption pattern, the onset potential only require 0.07 V to eliminate the increase in Gibbs free energy, and the NRR reaction can be carried out smoothly. Such a smaller onset potential means that it is very easy for nitrogen reduction into ammonia at ambient conditions.

Furthermore, in order to enhance the understanding of the reaction mechanism, it is also vital to find out the transition states in the reaction pathway. Figure 7 shows the structures and energies of the Transition States (TS) in the minimum energy pathway over the reaction pathway V with side-on pattern. It's easy to find that the maximum free energy barrier of 0.50 eV lies in the second PCET processes ($^*\text{N}-^*\text{NH} + \text{H}^+/\text{e}^- \rightarrow ^*\text{NH}-^*\text{NH}$), i.e. TS2. As for the rest of the reaction processes, the free energy barriers are all lower than that of TS2. The free energy barriers for TS1, TS4 and TS5 are only 0.06 eV, 0.12 eV and 0.01 eV, respectively. At the same time, there is no barrier for TS3. Considering that the previous reactions have released energy of 0.38 eV, this step ($^*\text{N}-^*\text{NH} + \text{H}^+/\text{e}^- \rightarrow ^*\text{NH}-^*\text{NH}$) only requires 0.12 eV. That is to say, the extra energy input for the NRR reaction based on the reaction pathway V with side-on pattern only needs 0.12 eV.

Interestingly, as shown in Figure 2, the introduction of B atom into g- C_2N is found to be further extended the absorption edge to the infrared light region and enhance the visiblelight absorption efficiency slightly. The maximum absorption peak is located in 2.45 eV, indicating B/g- C_2 possess outstanding ability to absorb certain energies of visible light. And the smaller peak located at 1.20 eV originate from the doping of B atom. Due to the fact that the maximum free energy barrier is only 0.50 eV, photon energy absorbed by the B/g- C_2N is enough to overcome this barrier, highlighting that the outstanding catalytic performance of B/g- C_2N for NRR.

As seen from the figure 8 and S2, the bader charge anal-

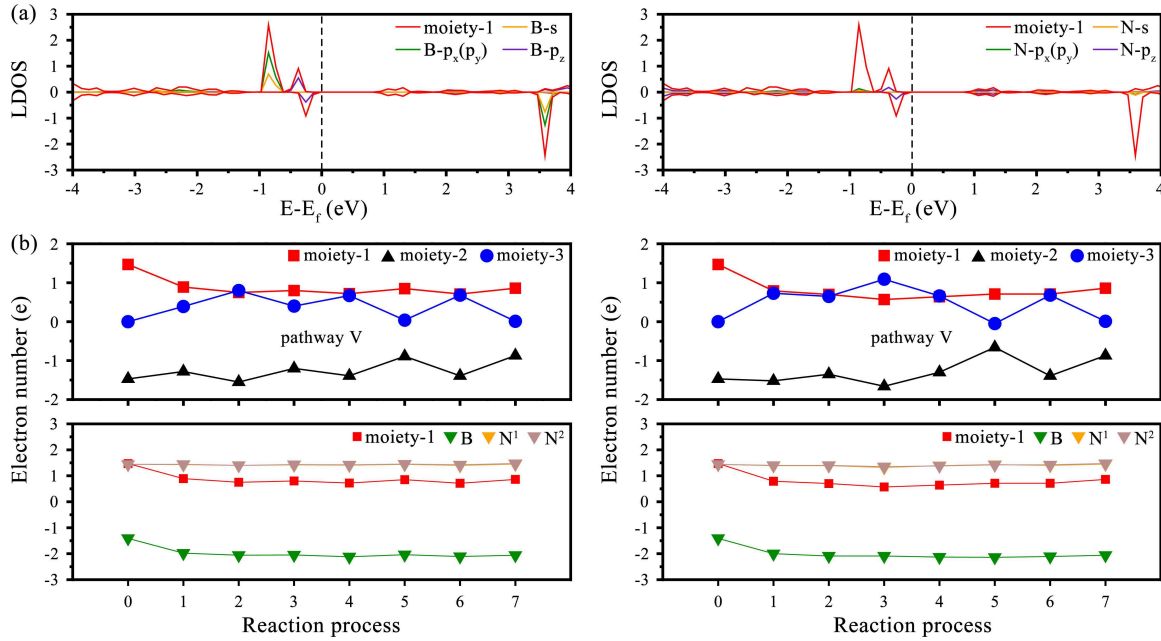


FIG. 8: (a) Spin-polarized local density of state (LDOS) of the moiety of BN₂. (b) Charge variation of the three moieties along the MERP (reaction pathway V) of N₂ with end-on (left) and side-on (right) adsorption configuration. The moiety-1, moiety-2 and moiety-3 represent BN₂ of B/g-C₂N, other parts of B/g-C₂N and adsorbed N₂, respectively. N¹ and N² are the N atom which bond to B atom. Reaction process 0, 1, 2, 3, 4, 5, 6, 7 represent the isolated state, N₂ adsorption reaction, initial, second, third, fourth, fifth and sixth protonation reaction, respectively.

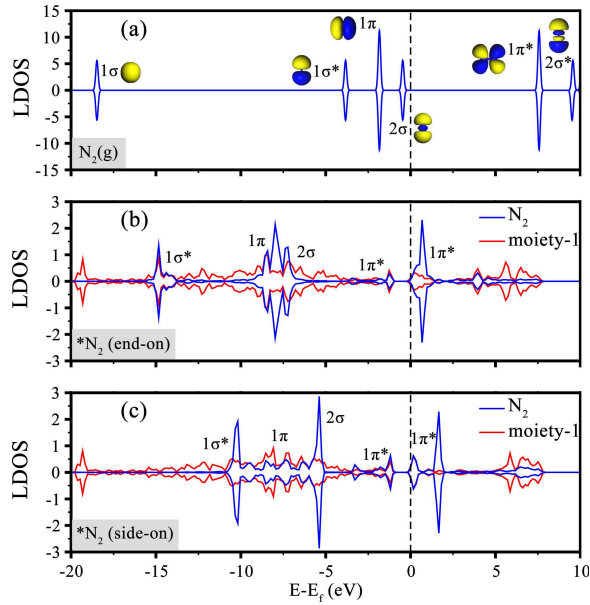


FIG. 9: Spin-polarized local density of state (LDOS) of (a) free N₂ molecule, N₂ adsorbed on B/g-C₂N with (b) end-on pattern and (c) side-on pattern. The blue and red lines represent the total LDOS of N₂ and BN₂ of B/g-C₂N (moiety-1), respectively. The Fermi level is set to 0 eV.

to N₂ are mainly come from the moiety of BN₂ of B/g-C₂N (moiety-1) when N₂ in initial adsorption whether end-on adsorption or side-on adsorption, indicating the BN₂ play the key role to capture and active N₂. Thereinto the B atom transfer more electrons to N₂ than the N atom of BN₂, because the occupied orbital (HOMO) and unoccupied orbital (LUMO+5) of BN₂ consist largely of s, $p_x(p_y)$ and p_z orbitals of B atom, besides, N₂ direct contact with B atom (figure 8a). However, in the course of the reaction, the BN₂ work as a transportation center to move the electrons of other parts of B/g-C₂N (moiety-2) which act as a electron reservoir to the N_xH_y (moiety-3), because the amounts of electrons for moiety-1 almost no change during the whole reaction. The introduction of B atom make g-C₂N can not only attract N₂ appropriately, but also carry the electrons of reservoir to the N₂ effectively.

In order to find out the origin of activity of B/g-C₂N, the local density of states (LDOS) of free N₂ molecule and B/g-C₂N with adsorbed N₂ molecule are calculated and shown in Figure 9. The molecular orbitals of free N₂ molecule mainly include 2 σ , 2 σ^* , 1 π , 3 σ , 1 π^* , and 3 σ^* molecular orbitals. When N₂ is adsorbed on B/g-C₂N, the molecular orbitals of N₂ will hybridize with the HOMO and LUMO of moiety-1 of B/g-C₂N intensively, as shown in figure 9b-c. For the end-on adsorption pattern, the 1 π^* orbital of N₂ can accept the electrons form the HOMO of moiety-1 of B/g-C₂N, leading the 1 π^* orbital is partially occupied, and the 2 σ^* ,

ysis of whole reaction show that the electrons of transfer

1π , 3σ orbitals can donate the electrons to the LUMO of moiety-1 of B/g-C₂N results in the decreases of their strength, further confirm the “acceptance-donation” interaction mechanism, the Bader charge analysis show that N₂ will get 0.39 |e| net charge from B/g-C₂N. As for side-on adsorption pattern, the $2\sigma^*$, 1π , 3σ orbitals have also changed and their strength also decreases, the difference is that the degree of the ionization of 1π orbital and the filling of $1\pi^*$ orbital are stronger, according with our previous research[49]. From the Bader charge analysis, we can find that N₂ will get 0.73 |e| net charge from B/g-C₂N, which means the $1\pi^*$ orbital of N₂ can accept more electrons from the HOMO of moiety-1 of B/g-C₂N in side-on adsorption pattern than end-on adsorption pattern, that’s why the difference of d_{N-N} , the longer d_{N-N} means the more active of N₂. So, the catalytic performance of B/g-C₂N with the side-on pattern of N₂ is the best reaction pathway.

Moreover, the stability of catalyst is also very important to the application in realistic case. We have examined the stability by using AIMD simulations. As shown in Figure S3, when temperature increases to 1000 K, the structure of B/g-C₂N is a slight of distortion in vertical plane, but a horizontal surface is still no great changes, showing the outstanding thermostability.

IV. CONCLUSION

In summary, we have demonstrated that B/g-C₂N can be a excellent photocatalyst for N₂ reduction to NH₃ by

performing the first-principles calculations. The calculated results indicate that the introduction of B atom to g-C₂N can not only maintain and improve slightly the optical absorption in the visible-light region relative to the pure g-C₂N, but also act as capture and activate center of N₂ through “acceptance-donation” mechanism. The low thermodynamics reaction free energy of 0.07 eV and free energy barrier of 0.50 eV, far below the photon energy absorbed by the B/g-C₂N, making B/g-C₂N as photocatalyst holds great potential for the reduction for the N₂ fixation. In addition, the strong binding energy offer high probability in terms of experimental synthesis. Furthermore, B/g-C₂N shows high thermal stability even though the temperature up to 1000 K.

Acknowledgments

This research is supported by the Natural Science Foundation of China (11375091), the Natural Science Foundation of Zhejiang (LY18A040003), the Natural Science Foundation of Ningbo (2018A610220), the K.C. Wong Magna Fund in Ningbo University. The computation is performed in the Supercomputer Center of NBU.

-
- [1] Rosca, V.; Duca, M.; de Groot, M. T.; Koper, M. T. Nitrogen Cycle Electrocatalysis. *Chem. Rev.* **2009**, *109*, 2209-2244.
 - [2] Licht, S.; Cui, B.; Wang, B. H.; Li, F. F.; Lau, J.; Liu, S. Z. Ammonia synthesis by N₂ and steam electrolysis in molten hydroxide suspensions of nanoscale Fe₂O₃. *Science* **2014**, *345*, 637-640.
 - [3] Smil, V. Detonator of the population explosion. *Nature* **1999**, *400*, 415.
 - [4] Service, R. F. Chemistry. New recipe produces ammonia from air, water, and sunlight. *Science (New York, NY)* **2014**, *345*, 610.
 - [5] Van der Ham, C. J. M.; Koper, M. T. M.; Hetterscheid, D. G. H. Challenges in reduction of dinitrogen by proton and electron transfer. *Chem. Soc. Rev.* **2014**, *43*, 5183-5191.
 - [6] Oshikiri, T.; Ueno, K.; Misawa, H. Selective Dinitrogen Conversion to Ammonia Using Water and Visible Light through Plasmon-induced Charge Separation. *Angew. Chem.* **2016**, *128*, 4010-4014.
 - [7] Kitano, M.; Inoue, Y.; Yamazaki, Y.; Hayashi, F.; Kanbara, S.; Matsuishi, S.; Yokoyama, T.; Kim, S. W.; Hara, M.; Hosono, H. Ammonia synthesis using a stable electrode as an electron donor and reversible hydrogen store. *Nat. Chem.* **2012**, *4*, 934-940.
 - [8] Seh, Z. W.; Kibsgaard, J.; Dickens, C. F.; Chorkendorff, I.; Nørskov, J. K.; Jaramillo, T. F. Combining theory and experiment in electrocatalysis: Insights into materials design. *Science* **2017**, *355*, eaad4998.
 - [9] Banerjee, A.; Yuhas, B. D.; Margulies, E. A.; Zhang, Y. B.; Shim, Y.; Wasielewski, M. R.; Kanatzidis, M. G. Photochemical Nitrogen Conversion to Ammonia in Ambient Conditions with FeMoS-Chalcogenides. *J. Am. Chem. Soc.* **2015**, *137*, 2030-2034.
 - [10] Bao, D.; Zhang, Q.; Meng, F. L.; Zhong, H. X.; Shi, M. M.; Zhang, Y.; Yan, J. M.; Jiang, Q.; Zhang, X. B. Electrochemical Reduction of N₂ under Ambient Conditions for Artificial N₂ Fixation and Renewable Energy Storage Using N₂/NH₃ Cycle. *Adv. Mater.* **2017**, *29*, 1604799.
 - [11] Sun, K.; Moreno-Hernandez, I. A.; Schmidt, W. C.; Zhou, X.; Crompton, J. C.; Liu, R.; Saadi, F. H.; Chen, Y.; Papadantonakis, K. M.; Lewis, N. S. A comparison of the chemical, optical and electrocatalytic properties of water-oxidation catalysts for use in integrated solar-fuel generators. *Energy Environ. Sci.* **2017**, *10*, 987-1002.
 - [12] Montoya, J. H.; Tsai, C.; Vojvodic, A.; Nørskov, J. K. The Challenge of Electrochemical Ammonia Synthesis: A New Perspective on the Role of Nitrogen Scaling Relations. *ChemSusChem* **2015**, *8*, 2180-2186.
 - [13] Azofra, L. M.; Li, N.; MacFarlane, D. R.; Sun, C. Promis-

- ing prospects for 2D d²-d⁴ M₃C₂ transition metal carbides (MXenes) in N₂ capture and conversion into ammonia. *Energy Environ. Sci.* **2016**,*9*,2545-2549 .
- [14] Yu, X.; Han, P.; Wei, Z.; Huang, L.; Gu, Z.; Peng, S.; Ma, J.; Zheng, G. Boron-Doped Graphene for Electrocatalytic N₂ Reduction. *Joule* **2018**,*2*,1610-1622.
- [15] Guo, C.; Ran, J.; Vasileff, A.; Qiao, S. Z. Rational design of electrocatalysts and photo(electro)catalysts for nitrogen reduction to ammonia (NH₃) under ambient conditions. *Energy Environ. Sci.* **2018**,*11*,45-56.
- [16] Qiu, W.; Xie, X. Y.; Qiu, J.; Fang, W. H.; Liang, R.; Ren, X.; Ji, X.; Cui, G.; Asiri, A. M.; Cui, G.; Tang, B.; Sun, X. High-performance artificial nitrogen fixation at ambient conditions using a metal-free electrocatalyst. *Nat. Commun.* **2018**,*9*,3485.
- [17] Tao, H.; Choi, C.; Ding, L. X.; Jiang, Z.; Han, Z.; Jia, M.; Fan, Q.; Gao, Y.; Wang, H.; Robertson, A. W.; Hong, S.; Jung, Y.; Liu, S.; Sun, Z. Nitrogen Fixation by Ru Single-Atom Electrocatalytic Reduction. *Chem* **2019**,*5*,204-214.
- [18] Qu, L.; Liu, Y.; Baek, J. B.; Dai, L. Nitrogen-Doped Graphene as Efficient Metal-Free Electrocatalyst for Oxygen Reduction in Fuel Cells. *ACS Nano* **2010**,*4*,1321-1326.
- [19] Liu, J.; Liu, Y.; Liu, N.; Han, Y.; Zhang, X.; Huang, H.; Lifshitz, Y.; Lee, S. T.; Zhong, J.; Kang, Z. Metal-free efficient photocatalyst for stable visible water splitting via a two-electron pathway. *Science* **2015**,*347*, 970-974.
- [20] Xu, Y.; Kraft, M.; Xu, R. Metal-free carbonaceous electrocatalysts and photocatalysts for water splitting. *Chem. Soc. Rev.* **2016**,*45*,3039-3052.
- [21] Yang, S.; Feng, X.; Wang, X.; Millen, K. Graphene-Based Carbon Nitride Nanosheets as Efficient Metal-Free Electrocatalysts for Oxygen Reduction Reactions. *Angew. Chem.* **2011**,*123*,5451-5455.
- [22] Zheng, Y.; Jiao, Y.; Zhu, Y.; Li, L. H.; Han, Y.; Chen, Y.; Qiao, S. Z. Hydrogen evolution by a metal-free electrocatalyst. *Nat. Commun.* **2014**,*5*,3783.
- [23] Xia, Z. Hydrogen evolution: Guiding principles. *Nature Energy* **2016**,*1*,16155.
- [24] He, J.; Wang, N.; Yang, Z.; Shen, X.; Wang, K.; Huang, C.; Li, Y. Fluoride graphdiyne as a free-standing electrode displaying ultra-stable and extraordinary high Li storage performance. *Energy Environ. Sci.* **2018**,*11*,2893-2903.
- [25] Zhao, Z.; Li, M.; Zhang, L.; Dai, L.; Xia, Z. Design Principles for Heteroatom-Doped Carbon Nanomaterials as Highly Efficient Catalysts for Fuel Cells and Metal-Air Batteries. *Adv. Mater.* **2015**,*27*,6834-6840.
- [26] Ran, J.; Guo, W.; Wang, H.; Zhu, B.; Yu, J.; Qiao, S. Z. Metal-Free 2D/2D Phosphorene/g-C₃N₄ Van der Waals Heterojunction for Highly Enhanced Visible-Light Photocatalytic H₂ Production. *Adv. Mater.* **2018**,*30*,1800128.
- [27] Lu, Z.; Chen, G.; Siahrostami, S.; Chen, Z.; Liu, K.; Xie, J.; Jaramillo, T. F. High-efficiency oxygen reduction to hydrogen peroxide catalysed by oxidized carbon materials. *Nature Catalysis* **2018**,*1*,156-162.
- [28] Xie, J.; Zhao, X.; Wu, M.; Li, Q.; Wang, Y.; Yao, J. Metal-Free Fluorine-Doped Carbon Electrocatalyst for CO₂ Reduction Outcompeting Hydrogen Evolution. *Angew. Chem. Int. Ed.* **2018**,*57*,9640-9644.
- [29] Ling, C.; Niu, X.; Li, Q.; Du, A.; Wang, J. Metal-Free Single Atom Catalyst for N₂ Fixation Driven by Visible Light. *J. Am. Chem. Soc.* **2018**,*140*,14161-14168.
- [30] Mahmood, J.; Lee, E. K.; Jung, M.; Shin, D.; Jeon, I. Y.; Jung, S. M.; Park, N. Nitrogenated holey two-dimensional structures. *Nature Communications* **2015**,*6*,6486.
- [31] Mahmood, J.; Li, F.; Jung, S. M.; Okyay, M. S.; Ahmad, I.; Kim, S. J.; Baek, J. B. An efficient and pH-universal ruthenium-based catalyst for the hydrogen evolution reaction. *Nature Nanotechnology* **2017**,*12*,441-446.
- [32] Zhang, X.; Chen, A.; Zhang, Z.; Jiao, M.; Zhou, Z. Transition metal anchored C₂N monolayers as efficient bifunctional electrocatalysts for hydrogen and oxygen evolution reactions. *J. Mater. Chem. A* **2018**,*6*,11446-11452 .
- [33] Wang, L.; Zheng, X.; Chen, L.; Xiong, Y.; Xu, H. Van der Waals Heterostructures Comprised of Ultrathin Polymer Nanosheets for Efficient Z-Scheme Overall Water Splitting. *Angew. Chem.* **2018**,*130*,3512-3516.
- [34] Zhang, X.; Chen, A.; Zhang, Z.; Zhou, Z. Double-atom catalysts: transition metal dimer-anchored C₂N monolayers as N₂ fixation electrocatalysts. *J. Mater. Chem. A* **2018**,*6*,18599-18604.
- [35] Kresse, G.; Furthmüller, J. Efficient iterative schemes for ab initio total-energy calculations using a plane-wave basis set. *Phys. Rev. B* **1996**,*54*,11169.
- [36] Kresse, G.; Joubert, D. From ultrasoft pseudopotentials to the projector augmented-wave method. *Phys. Rev. B* **1999**,*59*,1758.
- [37] Blöchl P.E. Projector augmented-wave method. *Phys. Rev. B* **1994**,*50*,17953.
- [38] Perdew, J. P.; Chevary, J. A.; Vosko, S. H.; Jackson, K. A.; Pederson, M. R.; Singh, D. J.; Fiollhais, C. Atoms, molecules, solids, and surfaces: Applications of the generalized gradient approximation for exchange and correlation. *Phys. Rev. B* **1992**,*46*,6671.
- [39] Perdew, J. P.; Wang, Y. Accurate and simple analytic representation of the electron-gas correlation energy. *Phys. Rev. B* **1992**,*45*,13244.
- [40] Grimme, S. Semiempirical GGA-type density functional constructed with a long-range dispersion correction. *J. Comput. Chem.* **2006**,*27*,1787-1799.
- [41] Heyd, J.; Scuseria, G. E.; Ernzerhof, M. Hybrid functionals based on a screened Coulomb potential. *J. Chem. Phys.* **2003**,*118*,8207-8215.
- [42] Henkelman, G.; Uberuaga, B. P.; Jónsson, H. A climbing image nudged elastic band method for finding saddle points and minimum energy paths. *J. Chem. Phys.* **2000**,*113*,9901-9904.
- [43] Nie, X.; Esopi, M. R.; Janik, M. J.; Asthagiri, A. Selectivity of CO₂ Reduction on Copper Electrodes: The Role of the Kinetics of Elementary Steps. *Angew. Chem. Int. Ed.* **2013**,*52*,2459-2462.
- [44] Rappe, A. K.; Casewit, C. J.; Colwell, K. S.; Iii, W. A.; Goddard, S.; Skiff, W. M. UFF, a full periodic table force field for molecular mechanics and molecular dynamics simulations. *J. Am. Chem. Soc.* **1992**,*114*,10024-10035.
- [45] Nørskov, J. K.; Rossmeisl, J.; Logadottir, A.; Lindqvist, L.; Kitchin, J. R.; Bligaard, T.; Jónsson, H. Origin of the Overpotential for Oxygen Reduction at a Fuel-Cell Cathode. *J. Phys. Chem. B* **2004**,*108*,17886-17892.
- [46] Rossmeisl, J.; Logadottir, A.; Nørskov, J. K. Electrolysis of water on oxidized metal surfaces. *Chem. Phys.* **2005**,*319*,178-184.
- [47] Zhang, H.; Zhang, X.; Yang, G.; Zhou, X. Point Defect Effects on Photoelectronic Properties of the

- Potential Metal-Free C₂N Photocatalysts: Insight from First-Principles Computations. *J. Phys. Chem. C* **2018**, *122*, 5291-5302.
- [48] Zhang, R.; Li, B.; Yang, J. Effects of stacking order, layer number and external electric field on electronic structures of few-layer C₂N-h₂D. *Nanoscale* **2015**, *7*, 14062-14070.
- [49] Zhu, H. R.; Hu, Y. L.; Wei, S. H.; Hua, D. Y. Single-Metal Atom Anchored on Boron Monolayer (β_{12}) as an Electrocatalyst for Nitrogen Reduction into Ammonia at Ambient Conditions: A First-Principles Study. *J. Phys. Chem. C* **2019**, *123*, 4274-4281.

Supporting Information

Single Boron Atom Anchored on graphitic carbon nitride nanosheet (B/g-C₂N) as a photocatalyst for Nitrogen fixation: A First-Principles Study

Hao-Ran Zhu,[†] Yan-Ling Hu,[†] Shi-Hao Wei,^{*,†} and Da-Yin Hua[‡]

[†]*Department of Microelectronic Science and Engineering, Faculty of Science, Ningbo University, Ningbo, 315211, P.R. China*

[‡]*Department of Physics, Faculty of Science, Ningbo University, Ningbo, 315211, P.R. China*

E-mail: weishihao@nbu.edu.cn

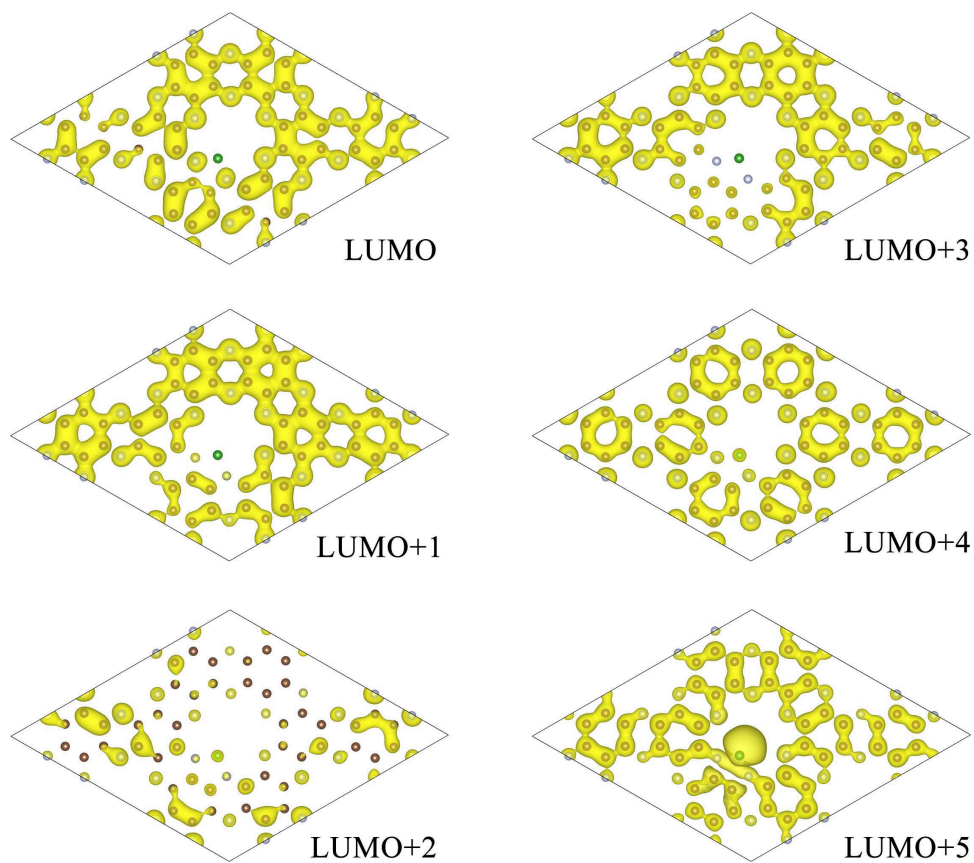


Figure S1: The lowest, second-lowest, third-lowest, fourth-lowest, fifth-lowest and sixth-lowest unoccupied molecular orbital (LUMO, LUMO+1, LUMO+2, LUMO+3, LUMO+4 and LUMO+5) of B/g-C₂N, where the isosurface value is set to be 0.001 e/Å³. The gray, lightpink, and blue balls represent C, B and N atoms, respectively.

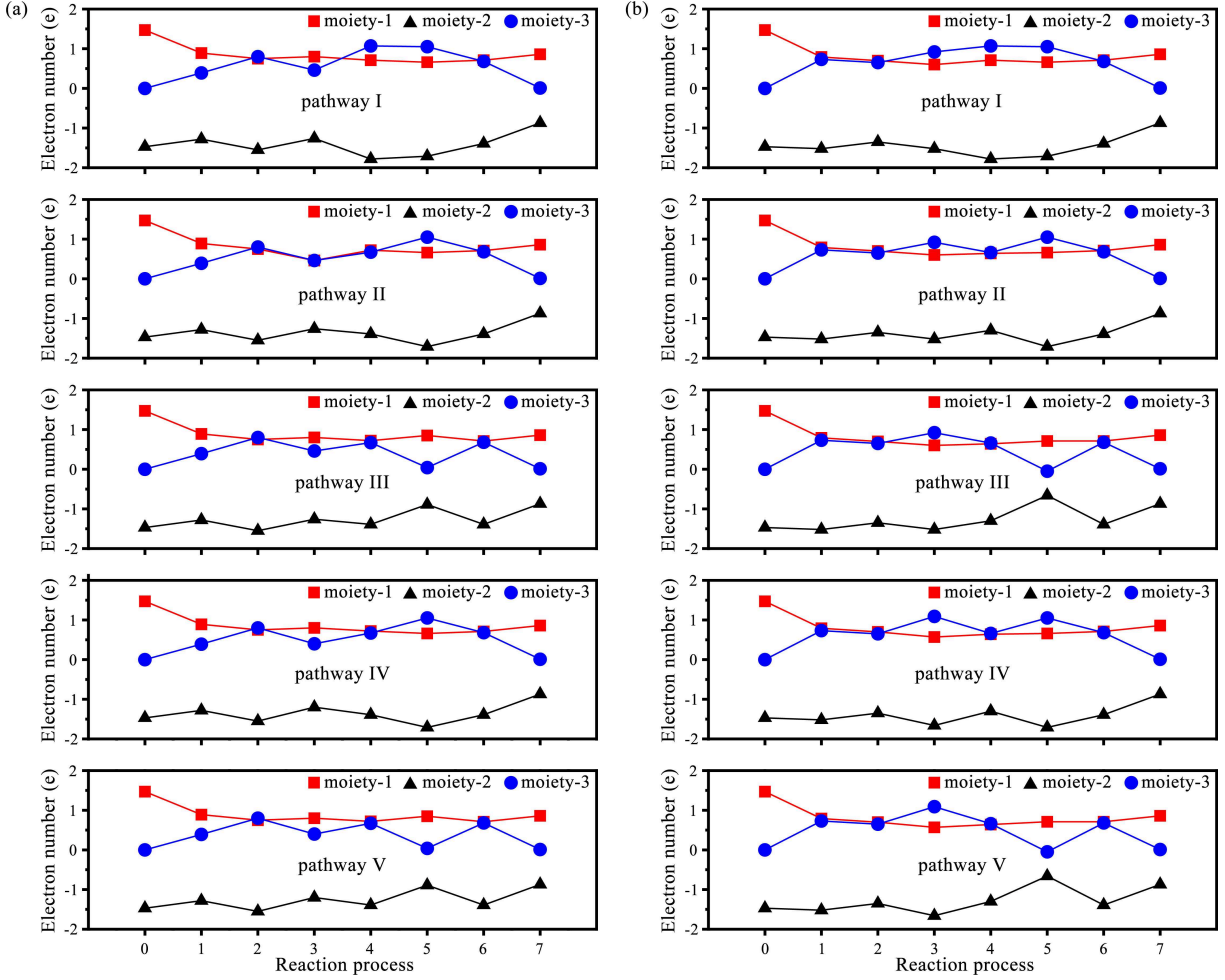


Figure S2: Charge variation of the three moieties along the N_2 adsorption pattern with (a) end-on adsorption pattern and (b) side-on adsorption pattern for all reaction pathways. The moiety-1, moiety-2 and moiety-3 represent BN_2 of B/g- C_2N , other parts of B/g- C_2N and adsorbed N_2 , respectively. Reaction process 0, 1, 2, 3, 4, 5, 6, 7 represent the isolated state, N_2 adsorption reaction, initial, second, third, fourth, fifth and sixth protonation reaction, respectively.

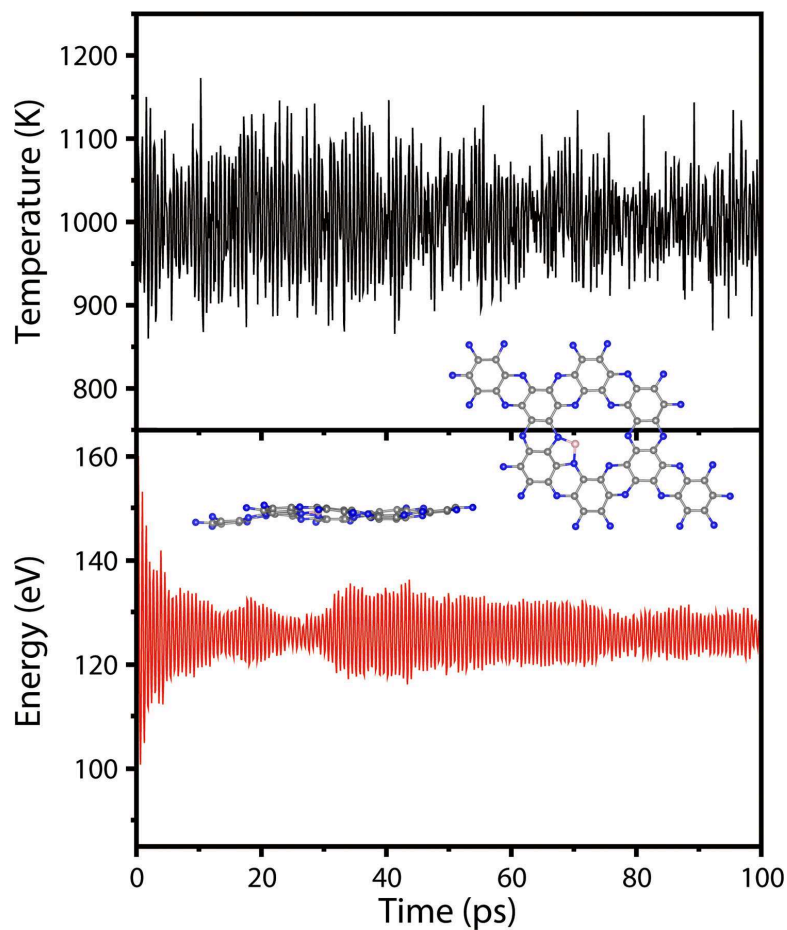


Figure S3: Variations of temperature and total energy of against the time for the molecular dynamics simulation of B/g-C₂N is carried out with a universal force field as implemented in Forcite code, insert are top and side views of the snapshot of atomic configuration. The simulation is run under 1000 K for 100 ps with a time step of 2 fs.